Moving Dirac nodes by chemical substitution

Niloufar Nilforoushan[a,1] (ID), Michele Casula[b,1] (ID), Adriano Amaricci[c,d] (ID), Marco Caputo[a,e], Jonathan Caillaux[a], Lama Khalil[a,f], Evangelos Papalazarou[a], Pascal Simon[a] (ID), Luca Perfetti[g] (ID), Ivana Vobornik[c] (ID), Pranab Kumar Das[c,h], Jun Fujii[c] (ID), Alexei Barinov[e], David Santos-Cottin[b], Yannick Klein[b] (ID), Michele Fabrizio[d] (ID), Andrea Gauzzi[b], and Marino Marsi[a,1] (ID)

[a]Laboratoire de Physique des Solides, Université Paris-Saclay, CNRS, 91405 Orsay, France; [b]Institut de Minéralogie de Physique des Matériaux et de Cosmochimie, Sorbonne Université, CNRS UMR 7590, Museum National d'Histoire Naturelle, 75252 Paris, France; [c]Istituto Officina dei Materiali, Consiglio Nazionale delle Ricerche, 34149 Trieste, Italy; [d]International School for Advanced Studies (SISSA), 34136 Trieste, Italy; [e]Elettra Sincrotrone Trieste, Area Science Park, 34149 Trieste, Italy; [f]Synchrotron SOLEIL, Gif-sur-Yvette F-91192, France; [g]Laboratoire des Solides Irradiés, CEA/DRF/IRAMIS, CNRS, Ecole Polytechnique, Institut Polytechnique de Paris, 91128 Palaiseau, France; and [h]International Centre for Theoretical Physics, 34151 Trieste, Italy

Dirac fermions play a central role in the study of topological phases, for they can generate a variety of exotic states, such as Weyl semimetals and topological insulators. The control and manipulation of Dirac fermions constitute a fundamental step toward the realization of novel concepts of electronic devices and quantum computation. By means of Angle-Resolved Photo-Emission Spectroscopy (ARPES) experiments and ab initio simulations, here, we show that Dirac states can be effectively tuned by doping a transition metal sulfide, BaNiS$_2$, through Co/Ni substitution. The symmetry and chemical characteristics of this material, combined with the modification of the charge-transfer gap of BaCo$_{1-x}$Ni$_x$S$_2$ across its phase diagram, lead to the formation of Dirac lines, whose position in k-space can be displaced along the $\Gamma - M$ symmetry direction and their form reshaped. Not only does the doping x tailor the location and shape of the Dirac bands, but it also controls the metal-insulator transition in the same compound, making BaCo$_{1-x}$Ni$_x$S$_2$ a model system to functionalize Dirac materials by varying the strength of electron correlations.

Dirac semi-metals | correlated electronic systems | functional topological materials

In the vast domain of topological Dirac and Weyl materials (1–9), the study of various underlying mechanisms (10–15) leading to the formation of nontrivial band structures is key to discovering new topological electronic states (16–23). A highly desirable feature of these materials is the tunability of the topological properties by an external parameter, which will make them suitable in view of technological applications, such as topological field-effect transistors (24). While a thorough control of band topology can be achieved, in principle, in optical lattices (25) and photonic crystals (26) through the wandering, merging, and reshaping of nodal points and lines in **k**-space (27, 28), in solid-state systems, such a control is much harder to achieve. Proposals have been made by using optical cavities (29), twisted van der Waals heterostructures (30), intercalation (31), chemical deposition (32, 33), impurities (34), and magnetic and electric applied fields (35), both static (36) and time-periodic (17, 37). Here, we prove that it is possible to move and reshape Dirac nodal lines in reciprocal space by chemical substitution. Namely, by means of Angle-Resolved Photo-Emission Spectroscopy (ARPES) experiments and ab initio simulations, we observe a sizable shift of robust massive Dirac nodes toward Γ in BaCo$_{1-x}$Ni$_x$S$_2$ as a function of doping x, obtained by replacing Ni with Co. At variance with previous attempts of controlling Dirac states by doping (19, 38), in our work, we report both a reshape and a significant **k**-displacement of the Dirac nodes.

BaCo$_{1-x}$Ni$_x$S$_2$ is a prototypical transition metal system with a simple square lattice (39). In BaCo$_{1-x}$Ni$_x$S$_2$, the same doping parameter x that tunes the position of the Dirac nodes also controls the electronic phase diagram, which features a first-order metal-insulator transition (MIT) at a critical substitution level, $x_{cr} \sim 0.22$ (40, 41), as shown in Fig. 1A. The Co rich side

($x = 0$) is an insulator with columnar antiferromagnetic (AF) order and with local moments in a high-spin ($S = 3/2$) configuration (42). This phase can be seen as a spin density wave (SDW) made of antiferromagnetically coupled collinear spin chains. Both electron-correlation strength and charge-transfer gap Δ_{CT} increase with decreasing x, as typically found in the late-transition metal series. The MIT at $x = 0.22$ is of interest because it is driven by electron correlations (43) and is associated with a competition between an insulating antiferromagnetic phase and an unconventional paramagnetic semimetal (44), where the Dirac nodes are found at the Fermi level. We show that a distinctive feature of these Dirac states is their dominant d-orbital character and that the underlying band-inversion mechanism is driven by a large $d - p$ hybridization combined with the nonsymmorphic symmetry (NSS) of the crystal (Fig. 1B). It follows that an essential role in controlling the properties of Dirac states is played by electron correlations and by the charge-transfer gap (Fig. 1C), as they have a direct impact on the hybridization strength. This results into an effective tunability of shape, energy, and wave vector of the Dirac lines in the proximity of the Fermi level. Specifically, the present ARPES study unveils Dirac bands moving from M to Γ with decreasing x. The bands are well explained quantitatively by ab initio calculations, in a hybrid density functional approximation suitable for including nonlocal correlations of screened-exchange

Significance

The on-demand control of topological properties with readily modifiable parameters is a fundamental step toward the design of novel electronic and spintronic devices. Here, we show that this goal can be achieved in the correlated system BaCo$_{1-x}$Ni$_x$S$_2$, where we succeeded in significantly changing the reciprocal space position and shape of Dirac nodes by chemically substituting Ni with Co. We prove that the tunability of the Dirac states is realized by varying the electron-correlation strength and the charge-transfer gap, both sensitive to the substitution level, x. Based on our finding, a class of late-transition metal compounds can be established as prototypical for engineering highly tunable Dirac materials.

APPLIED PHYSICAL SCIENCES

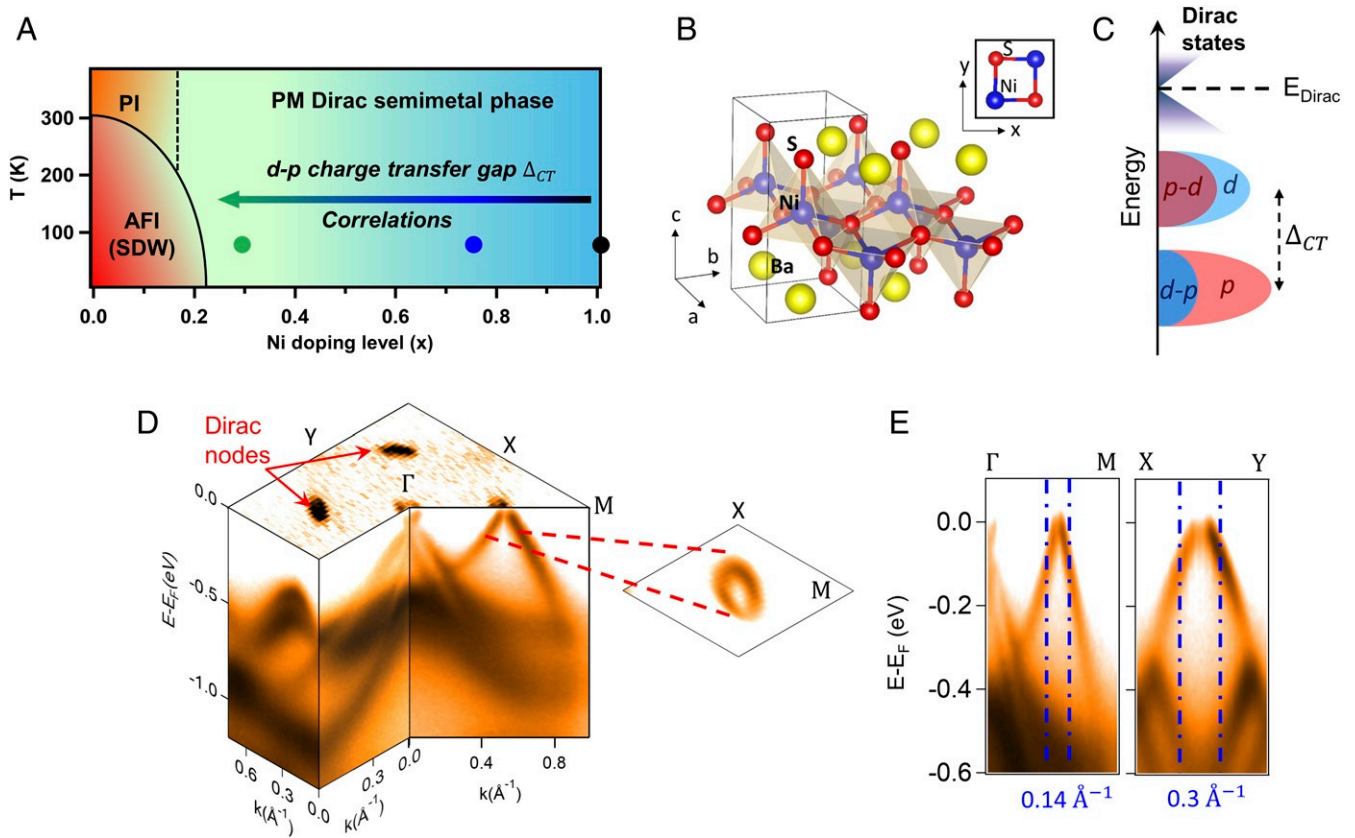**Fig. 1.** Experimental observation of Dirac states in the phase diagram of $BaCo_{1-x}Ni_xS_2$. (*A*) Phase diagram of $BaCo_{1-x}Ni_xS_2$. The transition lines between the PM, the paramagnetic insulator (PI), and the antiferromagnetic insulator (AFI) are reported. Colored circles indicate the different doping levels x studied in this work. This doping alters the $d-p$ charge-transfer gap (Δ_{CT}). (*B*) Crystal structure of $BaNiS_2$. Blue, red, and yellow spheres represent the Ni, S, and Ba atoms, respectively. The tetragonal unit cell is indicated by black solid lines. Lattice parameters are a = 4.44 Å and c = 8.93 Å (45). (*B, Upper*) Projection of the unit cell in the xy plane, containing two Ni atoms. (*C*) Schematics of the energy levels. The hybridization of $d-$ and $p-$ orbitals creates the Dirac states, and the $d-p$ charge-transfer gap fixes the position of these states in the $E-k$ space. (*D*) A three-dimensional ARPES map of $BaNiS_2$ ($x=1$) taken at 70-eV photon energy. The top surface shows the Fermi surface, and the sides of the cube present the band dispersion along high-symmetry directions. The linearly dispersing bands along $\Gamma-M$ cross each other at the Fermi level, E_F, thus creating four Dirac nodes. (*E*) We observe the oval-shaped section of the linearly dispersing bands on the k_x-k_y plane for $E-E_F = -100$ meV. The linearly dispersing bands along the major and minor axis of the oval are also shown.

type, which affect the hybridization between the d and p states. The same functional is able to describe the insulating SDW phase at $x=0$, driven by local correlations, upon increase of the optimal screened-exchange fraction. These calculations confirm that the Dirac nodes mobility in **k**-space stems directly from the evolution of the charge-transfer gap, i.e., the relative position between d and p on-site energies. These results clearly suggest that $BaCo_{1-x}Ni_xS_2$ is a model system to tailor Dirac states and, more generally, that two archetypal features of correlated systems, such as the hybrid $d-p$ bands and the charge-transfer gap, constitute a promising playground to engineer Dirac and topological materials using chemical substitution and other macroscopic control parameters.

Observation of Dirac States in BaNiS$_2$

We begin with the undoped sample $BaNiS_2$. In Fig. 1*D*, we represent a three-dimensional ARPES map of the Brillouin zone (BZ) for the high-symmetry directions. Along $\Gamma-M$, we observe linearly dispersing bands and—within ARPES resolution—gapless nodes at the Fermi level E_F. The Fermi surface reveals two pairs of such Dirac-like crossings related to each other by the time reversal and by the twofold rotation axis C_2 of the C_{2v} little group for the **k**-vectors along $\Gamma-M$. The Dirac nodes lie on the σ_d reflection planes and extend along the k_z direction, piercing the whole BZ, unlike other topological node-line

semimetals known to date, like Cu_3NPd (46, 47), Ca_3P_2 (48), and ZrSiS (49), where the nodal lines form closed areas around high-symmetry points.

As one can see in Fig. 1*E*, along the $\Gamma-M$ direction, the linearly dispersing bands remain isolated up to about $E-E_F = -0.35$ eV. These bands create an oval-shaped section on the constant energy maps near the Fermi level (Fig. 1*D*). This asymmetry, clearly visible in Fig. 1*E*, arises from the tilted type-I nature of the Dirac cone. The model Hamiltonian explaining the low-energy spectrum of the linearly dispersing bands observed experimentally is described in *SI Appendix*, c.f. section S1. The linear bands present no k_z dispersion, as shown in *SI Appendix*, section S2 and Fig. S2. The absence of dispersion is an indication of the two-dimensional (2D) nature of the Dirac cones. The Dirac point remains pinned almost at the Fermi level—about 30 meV above—and its wave vector is fixed along the $\Gamma(Z)-M(A)$ direction. Here, the Dirac point position is obtained by extrapolating the ARPES data. These values are in perfect agreement with those directly measured in a recent pump-probe experiment (50).

Symmetry Analysis of the Electronic Bands: Mechanism of Band Inversion and Formation of Dirac States

To unveil the physical mechanism responsible for the formation of Dirac cones in $BaNiS_2$, we performed a detailed theoretical

analysis of the symmetry of the electronic bands. We carried out density functional theory (DFT) calculations, by employing a modified Heyd–Scuseria–Ernzerhof (HSE) functional. The details of the band structure are presented in *Materials and Methods* and *SI Appendix*, section S3, where we also discuss how the inclusion of the spin-orbit coupling (SOC) affects the topological properties. The use of the HSE functional is dictated by nonlocal correlation effects present in this material. Indeed, a hybrid HSE functional with the optimal screened-exchange fraction $\alpha = 7\%$ (Eq. **1**) is needed to account for the Fermi surface renormalization of $BaNiS_2$ seen in quantum oscillations (51). Previous theoretical calculations (41, 52, 53) have shown that both S $3p$- and Ni $3d$-orbitals contribute to the Bloch functions near the Fermi level. We ascribe the electronic states close to the Fermi level mainly to the Ni $3d$-orbitals hybridized with the S $3p$-orbitals. In this situation, the exchange contribution to the hybridization with the ligands plays a crucial role in determining the topology of the Fermi surface (*SI Appendix*, Fig. S6B illustrates the electronic structure dependence upon α). Hereafter, we consider a Cartesian reference frame where the x and y axes are parallel to the Ni–S bonds in the tetragonal ab-plane. Neighboring Ni ions are aligned along the diagonal xy direction (Fig. 1B). In this frame, at the crossing points, located along the (u, u, v) directions, the bands have dominant d_{z^2} and $d_{x^2-y^2}$ character. This multiorbital nature was confirmed by a polarization-dependent laser-ARPES study (*SI Appendix*, section S4).

As sketched in Fig. 2A, the crystal structure of $BaNiS_2$ is made of square-lattice layers of staggered, edge-sharing NiS_5 pyramids pointing along the out-of-plane [001] c-axis direction (40). The Ni atoms inside the S pyramids probe a crystal field that splits the atomic d-shell into the following levels (in descending energy order): $d_{x^2-y^2}$, d_{z^2}, the degenerate doublet (d_{xz}, d_{yz}), and d_{xy}. Due to the $3d^8 4s^0$ electronic configuration of the Ni^{2+} ion, we expect all d-orbitals to be filled, except the two highest ones, $d_{x^2-y^2}$ and d_{z^2}, which are nearly half-filled, assuming that the Hund's exchange is sufficiently strong.

The puckering of the $BaNiS_2$ layers gives rise to a tetragonal nonsymmorphic $P4/nmm$ structure characterized by a horizontal gliding plane, which generates two Ni and two apical S positions at (1/4, 1/4, z) and (3/4, 3/4, $-z$), separated by a fractional $\mathbf{f} =$ (1/2, 1/2, 0) translation in the plane (Fig. 2A). The two Ni atoms occupy Wyckoff position $2c$, corresponding to the M symmetry, while the two planar S atoms are at the $2a$ site, corresponding to the Γ symmetry.

At M, the energy hierarchy of the atomic orbitals follows closely the crystal field splitting (Fig. 2B). The little group admits the following four 2D irreducible representations (irreps): $E_{Mi=1,...,4}$ (54), each originating from the same orbitals of the two inequivalent Ni. However, the levels stacking at Γ, whose little group is isomorphic to D_{4h}, differ from that predicted by the crystal field. This is due to the sizable hybridization of Ni d-orbitals with the S p ligands (*SI Appendix*, section S5). Owing to the NSS, each Bloch eigenfunction at Γ is either even or odd
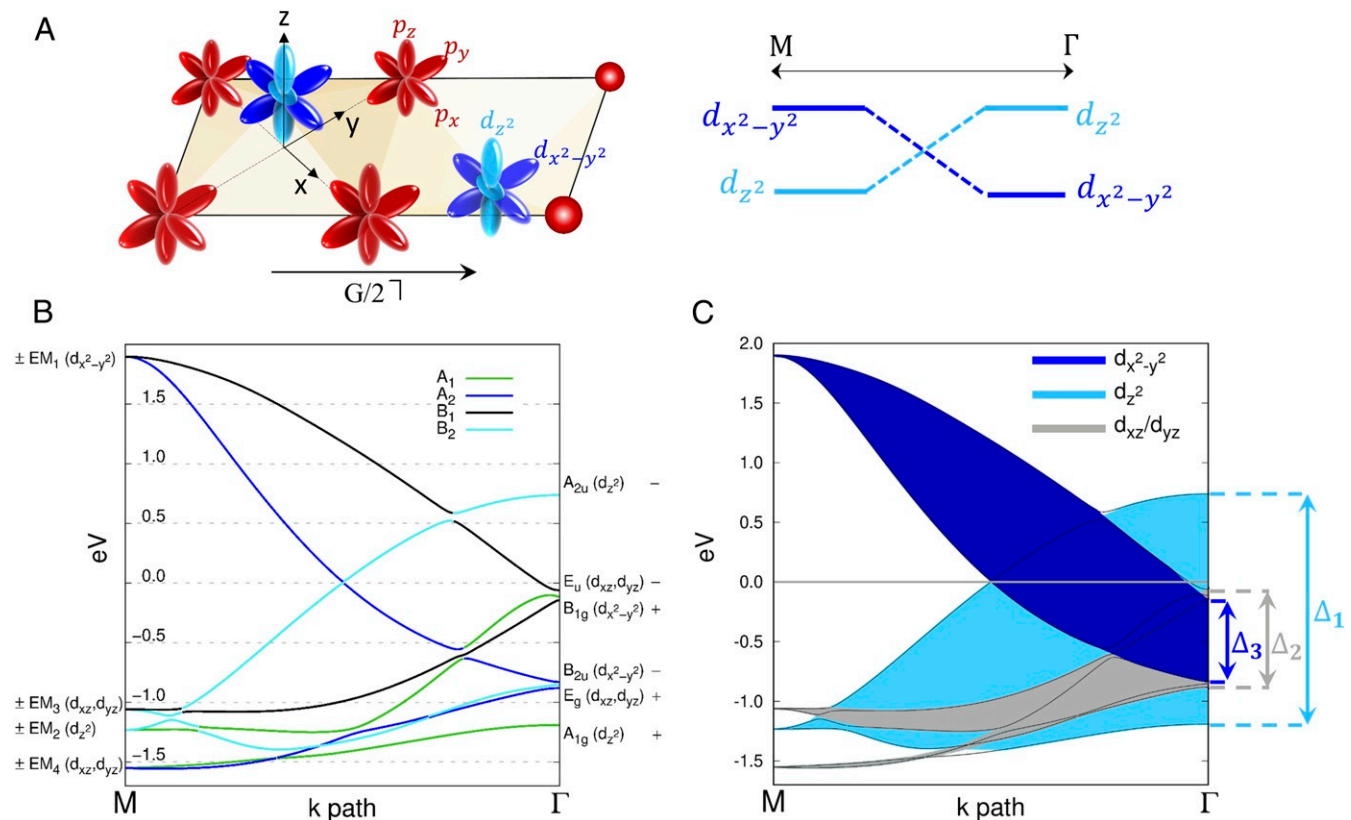

Fig. 2. Mechanism of band inversion and formation of hybridized Dirac states. (*A*) Schematics of the d- and p-orbitals of Ni and S, respectively. (*A, Right*) The strong hybridization of the d-orbitals with the ligand p-orbitals, favored by the NSS, is responsible for the band inversion. (*B*) Band symmetries along the MΓ direction. At the right-hand (left-hand) side, we report the symmetries at Γ (M), while the symmetries in between follow the irreps of the C_{2v} point group, represented by the color code in the key. The outer $+/-$ signs indicate the parity of the respective Bloch wave functions at the beginning and at the end of the **k**-path. (*C*) Evolution of the energy splitting between even and odd combinations of d-orbitals along MΓ. The dominant orbital character is reported. The navy blue (blue) vertical arrows indicate the splitting Δ_3 (Δ_1) between the $d_{x^2-y^2}$ (d_{z^2}) bands at Γ due to the hybridization with the ligand p_z-orbitals. The gray arrow indicates the splitting Δ_2 of d_{xz}/d_{yz} bands at Γ due to their hybridization with the p_x/p_y orbitals.

upon exchanging the inequivalent Ni and S within each unit cell. Even and odd combinations of identical d-orbitals belonging to inequivalent Ni atoms split in energy since they hybridize differently with the ligands. The even combination of the $d_{x^2-y^2}$ Ni orbitals is weakly hybridized with the p_z-orbitals of the planar S, since the two Ni atoms are out of the basal plane. On the other hand, the odd combination is nonbonding. It follows that the B_{1g} even combination shifts up in energy with respect to the B_{2u} odd one. Seemingly, the A_{2u} odd combination of the d_{z^2}-orbitals hybridizes substantially with the p_z-orbitals of the planar and apical S, thus increasing significantly the energy of the odd combination. Eventually, its energy raises above the B_{1g} and B_{2u} levels, as well as the A_{1g} state (even combination of d_{z^2}-orbitals). This leads to a reverse of the crystal field order, as reported in Fig. 2C.

Because the irreps at the A and Z **k**-points are equivalent to those at M and Γ (54), respectively, the orbital hierarchy found at M and Γ must be preserved along the $M - A$ and $\Gamma - Z$ directions. Thus, for any v along the $(0, 0, v) \rightarrow (1/2, 1/2, v)$ path, a band inversion between bands with predominant d_{z^2} and $d_{x^2-y^2}$ characters must occur. Therefore, band crossing is allowed without SOC and leads to two Dirac points at a given k_z right at the Fermi energy for $k_z = 0$. Indeed, the crossing bands transform like different irreps of the little group, which is isomorphic to C_{2v} for a **k**-point (u, u, v) with $v = 0, 1/2$, and to C_s with $v \in \,]0, 1/2 \, [$. These Dirac nodes are massive as a consequence of the SOC, which makes the material a weak topological insulator. The SOC gap is, however, very small (about 18 meV) and below ARPES resolution. Nevertheless, the focus of the present work is not on these very-low-energy features, but, rather, on the tunability of the whole Dirac nodal structure. In the family of weak topological insulators having the same $P4/nmm$ space group and showing SOC-gapped Dirac cones along the $\Gamma - M$ direction (such as ZrSiS, for instance), $BaCo_{1-x}Ni_xS_2$ is a peculiar member. Indeed, the strong local Hund's exchange coupling favors nearly half-filled $d_{x^2-y^2}$ and d_{z^2} orbitals, which explains the proximity of the Dirac nodes to the Fermi level for $x = 1$, in accordance also to Luttinger's theorem (*SI Appendix*, section S6). This is another signature of the relevance of electron correlations in this transition-metal compound, which manifest themselves in both local and nonlocal contributions, the former leading eventually to the insulating phase at the Co side of $BaCo_{1-x}Ni_xS_2$ and the latter affecting the variation of Δ_{CT} across the series.

ARPES Evidence of Dirac States Tuned by Doping, *x*

We now turn our attention to the effect of the Co/Ni substitution on the evolution of the band structure, notably, the Dirac states. According to the $BaCo_{1-x}Ni_xS_2$ phase diagram, this substitution modifies the strength of the electron–electron correlations and the amplitude of Δ_{CT}. A series of ARPES spectra are given for the $x = 0.75$ and $x = 0.3$ compositions. In Fig. 3, we display the evolution of the Fermi surface and the electronic band structure along $\Gamma - M$ with x. For $x = 0.75$, the Fermi surface is composed of a four-leaf feature at the Γ point and four hole-like pockets along the $\Gamma - M$ (Fig. 3C). These pockets originate from the Dirac states crossing the Fermi level. The Dirac cone is shown in Fig. 3D along and perpendicular to the $\Gamma - M$ direction. At higher substitution levels, for $x = 0.30$, the Dirac states shift up to lower binding energies, so the size of the hole-like pockets in the $k_x - k_y$ plane is increased (Fig. 3 E and F). The ARPES signal is also broader: Since our structural study indicates that the crystalline quality is not affected by Co/Ni substitution (*SI Appendix*, section S7 and Table S2), this broadening is consistent with the increase in electron–electron correlations while approaching the MIT (39, 43, 52). On the theoretical ground, this is expected because Co substitution brings the whole d-manifold closer to fillings where local correlation effects are enhanced, according

to the Hund's metals picture (55). Fig. 4A schematically illustrates the evolution of the Dirac cone with x; in Table 1, we give the position of the Dirac points determined by extrapolating the band dispersion. In summary, one notes that the Co substitution moves the Dirac points further beyond the Fermi level and reduces its wave vector.

Evolution of Dirac States with Doping

In order to account for the tunability of the Dirac cones detected by ARPES, we carried out extensive ab initio DFT-HSE calculations as a function of the screened-exchange fraction α, which controls the correlation strength in the modified hybrid functional framework. To explicitly include the charge transfer Δ_{CT} variation led by chemical substitution, we computed the two end-members of the $BaCo_{1-x}Ni_xS_2$ series, namely, $x = 1$ ($BaNiS_2$) and $x = 0$ ($BaCoS_2$). For $x = 1$, the optimal $\alpha = 7\%$, since it reproduces the frequencies of quantum oscillations in $BaNiS_2$ (51). In order to fix such percentage for $x = 0$, we performed ab initio calculations assuming the collinear SDW observed experimentally (42), by means of both HSE and the generalized gradient approximation supplemented by local Hubbard interactions (GGA+U). The strength of the Hubbard repulsion $U = 3.0$ eV and local Hund's coupling $J = 0.9$ eV, included in GGA+U, was estimated from first principles within the constrained random phase approximation (43). GGA+U correctly predicted an insulating state (Fig. 4E). By varying the percentage α of screened exchange in HSE, we found that, while $\alpha = 7\%$ gives a metal, $\alpha \simeq 19\%$ reproduces the main peaks across the gap obtained by GGA+U (Fig. 4E). This result suggests that HSE can describe $BaCo_{1-x}Ni_xS_2$ only if the percentage of screened exchange α increases from 7% up to around 19% with decreasing x from one to zero. Starting from the most correlated Co side, the reduction of the Hubbard repulsion upon electron doping, implied by the α dependence on x, has been found in other strongly correlated compounds, such as La-doped Sr_2IrO_4 (56).

In $BaCoS_2$, besides the SDW solution compatible with the observed low-temperature state, it is possible to obtain another one once magnetism is not allowed, namely, forcing spin $SU(2)$ symmetry. This paramagnetic metal (PM) phase is metastable at low temperature and adiabatically connected with the metallic solution at $x = 1$. Therefore, it hosts Dirac cones and is separated by an energy barrier from the stable insulating SDW phase. In Fig. 4D, we plot the distance of the Dirac node ($\mathbf{k}_{Dirac}$) from the Γ point as a function of α, for $x = 1$ and the metallic solution at $x = 0$. $\mathbf{k}_{Dirac}$ strongly depends on both x and α (*SI Appendix*, section S8 and Fig. S6 *A and B* plot the band structures where the $\mathbf{k}_{Dirac}$ values have been extracted from). By taking the optimal α's for each x, the Dirac node is predicted to drift from $\mathbf{k}_{Dirac} \simeq 0.52 \, \text{Å}^{-1}$ at $x = 1$ down to $\mathbf{k}_{Dirac} \simeq 0.38 \, \text{Å}^{-1}$ at $x = 0$, covering the colored y-axis range in Fig. 4D, in agreement with the range of variation seen in experiment.

Next, we analyzed the 22-bands full $d - p$ tight-binding (TB) model derived from the ab initio DFT-HSE for $x = 1$ (with $\alpha = 7\%$) and for $x = 0$ (with $\alpha = 19\%$); c.f. *SI Appendix*, section S9 and Fig. S8. The $x = 0$ state has shifted Dirac cones in both **k** and energy position with respect to the $BaNiS_2$ parent compound. To underpin the mechanism behind the evolution of the cones, we compared the two TB Hamiltonians for $x = 0$ and $x = 1$. The main difference involves the on-site energies and, in particular, the relative position of the p and d states, i.e., the charge-transfer gap Δ_{CT}. This proves that the doping x via chemical substitution is indeed an effective control parameter, as it alters the $d - p$ charge-transfer gap Δ_{CT} together with the correlation strength and, consequently, the $d - p$ hybridization amplitude, which directly affects the position and shape of the Dirac nodes.
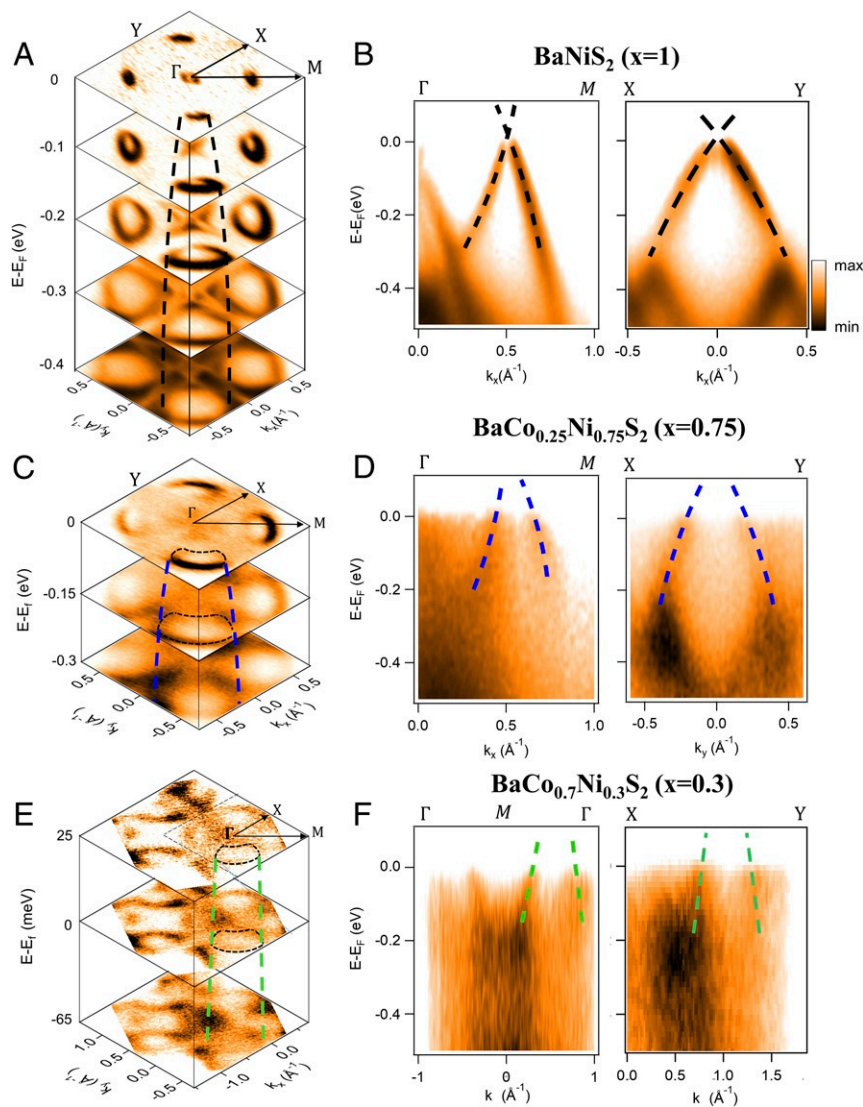
Fig. 3. Experimental ARPES evolution of Dirac states with doping x, in BaCo$_{1-x}$Ni$_x$S$_2$. (*A* and *B*) Dispersion of these states for $x = 1$. *A* shows the iso-energy contours with increasing binding energy. *B* shows the dispersion along the high-symmetry directions $\Gamma - M$ and $X - Y$. Note the anisotropy of the dispersion, which is due to the oval shape of the pockets at the Fermi surface. Dashed lines are a guide to the eye that represent schematically the dispersion. Panels *C* and *D* and panels *E* and *F* are the same as in *A* and *B* for the $x = 0.75$ and the $x = 0.3$ samples, respectively. All spectra are obtained with a photon energy of 70 eV.

In the following, we define Δ_{CT} as the energy difference between the average energy position of the full d manifold and the average one of the p manifold. According to our HSE calculations, Δ_{CT} varies from 1.1 eV ($x = 1$) to 1.6 eV ($x = 0$). Assuming a linear variation of Δ_{CT} and on-site energies upon Ni-content x, we are able to estimate $\Delta_{CT} = \Delta_{CT}(x)$ and, thus, predict the evolution of the band structure and Dirac states by interpolating between the BaCoS$_2$ and BaNiS$_2$ TB models. This evolution is reported in Fig. 4*B*, while the actual Dirac-states dynamics—represented by the behavior of both the **k** and energy position of the Dirac point as a function of Δ_{CT}—is plotted in Fig. 4*C*. This shows that the tunability upon doping found experimentally does not merely consist of a rigid shift of the Dirac cones (19), but it involves the change of both their shape and **k**-position (see also *SI Appendix*, Fig. S8).

This theoretical prediction is in good agreement with the observed evolution of the Dirac cone with x, as is apparent in Fig. 4*A*. Such movable Dirac nodes in the **k**-space have recently attracted a great deal of interest from theory (15, 28, 57), as well

as in the context of optical lattices (25) and photonic crystals (26). The present system offers the opportunity for observing in a real material how a simple experimental parameter—chemical substitution—can be used to tune Dirac states.

Manipulating the shape and position of the Dirac cones is also expected in BaCo$_{1-x}$Ni$_x$S$_2$ using pressure in bulk samples or strain in thin films. Specifically, strain can be used to distort the square lattice, thus breaking one of the symmetries that protect the fourfold Dirac nodal lines. Nontrivial phases, such as Weyl semimetals, could then be triggered by time-inversion breaking perturbations, like an external electromagnetic field. A further possibility is the creation of spin-chiral edge states, thanks to the proximity of the material to a topological insulator.

Conclusion

In conclusion, we have shown that BaCo$_{1-x}$Ni$_x$S$_2$ offers the opportunity of effectively tuning Dirac bands by exploiting a peculiar inversion mechanism of d-electron bands. Namely, the

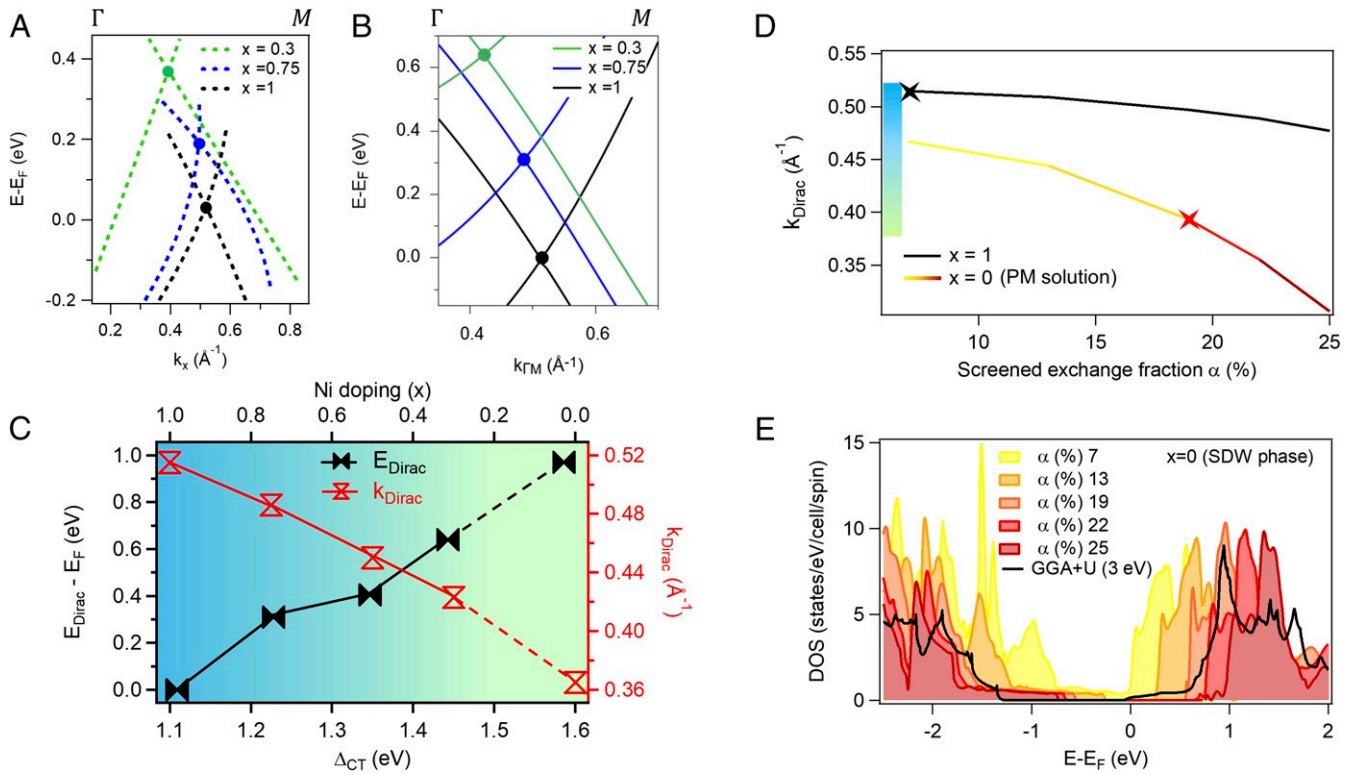Nilforoushan et al.
Moving Dirac nodes by chemical substitution

PNAS | 5 of 8
https://doi.org/10.1073/pnas.2108617118

Fig. 4. Evolution of Dirac states with doping x, in $BaCo_{1-x}Ni_xS_2$. (*A*) Curves fitting the experimental Dirac states for different values of x. (*B*) Evolution of the Dirac states predicted by our HSE/TB calculations of the band structure. (*C*) Variation of the charge-transfer gap, $\triangle_{CT}$, with the Ni content, x. The point at $x = 0$ is the metastable state adiabatically connected with the metallic phase found for $x > x_{cr} \simeq 0.22$. By reducing x from one to zero, the Dirac point, k_{Dirac}, moves toward Γ. Correspondingly, the difference between the energy of this point and the Fermi level increases. (*D*) k_{Dirac} variation for $x = 0$ and $x = 1$, when we relax the screened-exchange fraction parameter α in the modified HSE functional. The black (red) star is located at the value of α that optimally captures the correlation strength in $BaNiS_2$ ($BaCoS_2$), used to predict the evolution in B and C. (*E*) Density of states (DOS) of the $x = 0$ collinear SDW solution, as computed by GGA+U (black line) with ab initio values for the local Hubbard repulsion and the modified HSE with values for α covering different correlation strengths. Optimal $\alpha = 19\%$ best matches the GGA+U DOS.

Co/Ni substitution has been found to alter both the charge-transfer gap and the strength of the electron–electron correlations that control the position and shape of the bands. Remarkably, the same Co/Ni substitution makes it possible to span the electronic phase diagram, with the Dirac states present across its metallic phase. We emphasize the applicability of the present approach to a wide class of materials described by the $d - p$ effective Hamiltonian, thus enabling us to forge Dirac states controlled by chemical substitutions. This opens the perspective of engineering Dirac states in correlated electronic systems by exploiting macroscopically tunable parameters.

Materials and Methods

ARPES Measurements. Single crystals of $BaCo_{1-x}Ni_xS_2$ were cleaved in situ, exposing the ab plane under ultrahigh vacuum (UHV) conditions (base pressure better than 10^{-11} mbar). Most of the synchrotron-radiation ARPES measurements were performed on the Advanced Photoelectric Effect beamline at the Elettra light source, with linearly polarized beam and different photon energies. The sample temperature was 70 K. The data were collected with a VG-DA30 Scienta hemispherical analyzer that operates in deflection mode and provides high-resolution 2D **k**-space mapping while the sample geometry is fixed (58). The total measured energy resolution was ~ 15 meV, and the angular resolution was better than $0.2°$. Some of the data were also acquired with a 6.2-eV laser source (59) and some at the Spectromicroscopy beamline (60): The end station hosted two exchangeable multilayer-coated Schwarzschild objectives designed to focus the radiation at 27 and 74 eV to a small spot (~ 600 nm). The photoelectrons were collected by an internal movable hemispherical electron-energy analyzer that can perform polar and azimuthal angular scans in UHV. The energy and momentum resolutions are ~ 33 meV and ~ 0.03 Å^{-1}, respectively.

Ab Initio Calculations. We carried out ab initio DFT calculations in a modified HSE functional. It improves upon the Perdew, Burke, and Ernzerhof (PBE) (61, 62) exchange-correlation (*xc*) functional by the addition of a screened Fock term ($E_x^{HF,screened}$), such that the resulting functional reads as

$$E_{xc}^{HSE} = E_{xc}^{PBE} + \alpha \left(E_x^{HF,screened}(\omega) - E_x^{PBE,screened}(\omega) \right). \qquad [1]$$

The screened interaction is written as: $V^{screened}(r) = \text{erfc}(\omega r)/r$, where erfc is the complementary error function, and $\omega = 0.108$ in atomic units, i.e., the HSE regular value. In this work, α is instead taken as an adjustable parameter, which depends on the correlation strength of the system.

We used the QUANTUM ESPRESSO package (63, 64) to perform modified HSE calculations for $BaNiS_2$ ($x = 1$) and $BaCoS_2$ ($x = 0$) in a plane-waves (PW) basis set. The geometry of the cell and the internal coordinates were taken from experiment (45). We replaced the core electrons of the Ni, Co, Ba, and S atoms by norm-conserving pseudopotentials. For the Ni (Co) pseudopotential, we used both fully- and scalar-relativistic versions, with 10 (9) valence electrons and nonlinear core corrections. The Ba pseudopotential includes the semicore states, while the S pseudopotential has $3s^2 3p^4$ in-valence electrons. We employed a $8 \times 8 \times 8$ electron-momentum grid and

Table 1. Position of the Dirac point (DP) in energy and momentum space for different doping levels in the metallic phase

Compound	E_{DP} (eV)	k_{DP} (Å^{-1})
$BaNiS_2$	0.03 ± 0.01	0.52 ± 0.01
$BaCo_{0.25}Ni_{0.75}S_2$	0.19 ± 0.01	0.49 ± 0.01
$BaCo_{0.7}Ni_{0.3}S_2$	0.37 ± 0.02	0.39 ± 0.02

a Methfessel–Paxton smearing of 0.01 Ry for the **k**-point integration. The PW cutoff was 60 Ry for the wave function. The nonlocal exchange terms of the HSE functional were computed through the fast implementation of the exact Fock energy (64), based on the adaptively compressed exchange scheme (65). In the nonlocal Fock operator evaluation, the integration over the **q**-points was down-sampled on an $8 \times 8 \times 2$ grid. We applied a half-a-grid shift in the z direction to minimize the number of nonequivalent momenta in the **k** + **q** grid. By means of the Wannier90 code (66), we performed a Wannier interpolation of the ab initio bands for both $x = 0$ and $x = 1$ in the energy window spanned by the $d - p$ manifold, to accurately resolve the band structure, chemical potential, and Fermi surface and to derive a minimal TB model.

To successfully deal with the most demanding simulations (HSE functional evaluated in a larger cell with spin-resolved orbitals), we supplemented the Quantum Espresso calculations with some performed by means of the Crystal17 package (67), particularly suited to efficiently compute the exact exchange operator. In this framework, we used scalar-relativistic Hartree–Fock energy-consistent pseudopotentials by Burkatzki, Filippi, and Dolg (68) and an adapted VTZ Gaussian basis set for both Ni and Co. In our Crystal17 calculations, the k-grid was set to a $32 \times 32 \times 32$ dense mesh, with a Fermi

smearing of 0.001 Hartree. We cross-checked the Crystal17 and Quantum Espresso band structures for the paramagnetic phase of $BaNiS_2$ and $BaCoS_2$, in order to verify the convergence of all relevant parameters in both PW and Gaussian DFT calculations.

Data Availability. All study data are included in the article and/or supporting information.

1. M. Z. Hasan, C. L. Kane, Colloquium: Topological insulators. *Rev. Mod. Phys.* **82**, 3045 (2010).
2. A. Bansil, H. Lin, T. Das, Colloquium: Topological band theory. *Rev. Mod. Phys.* **88**, 021004 (2016).
3. B. Bradlyn et al., Topological quantum chemistry. *Nature* **547**, 298–305 (2017).
4. N. P. Armitage, E. J. Mele, A. Vishwanath, Weyl and Dirac semimetals in three-dimensional solids. *Rev. Mod. Phys.* **90**, 15001 (2018).
5. Q. D. Gibson et al., Three-dimensional Dirac semimetals: Design principles and predictions of new materials. *Phys. Rev. B Condens. Matter Mater. Phys.* **91**, 205128 (2015).
6. M. G. Vergniory et al., A complete catalogue of high-quality topological materials. *Nature* **566**, 480–485 (2019).
7. Z. Wang et al., Dirac semimetal and topological phase transitions in A_3Bi (A=Na, K, Rb). *Phys. Rev. B Condens. Matter Mater. Phys.* **85**, 195320 (2012).
8. S. Borisenko et al., Experimental realization of a three-dimensional Dirac semimetal. *Phys. Rev. Lett.* **113**, 027603 (2014).
9. Z. K. Liu et al., A stable three-dimensional topological Dirac semimetal Cd_3As_2. *Nat. Mater.* **13**, 677–681 (2014).
10. L. Müchler et al., Topological insulators from a chemist's perspective. *Angew. Chem. Int. Ed. Engl.* **51**, 7221–7225 (2012).
11. C. L. Kane, E. J. Mele, Z_2 topological order and the quantum spin hall effect. *Phys. Rev. Lett.* **95**, 146802 (2005).
12. S. M. Young et al., Dirac semimetal in three dimensions. *Phys. Rev. Lett.* **108**, 140405 (2012).
13. S. M. Young, C. L. Kane, Dirac semimetals in two dimensions. *Phys. Rev. Lett.* **115**, 126803 (2015).
14. L. Muechler, A. Alexandradinata, T. Neupert, R. Car, Topological nonsymmorphic metals from band inversion. *Phys. Rev. X* **6**, 041069 (2016).
15. B. J. Yang, N. Nagaosa, Classification of stable three-dimensional Dirac semimetals with nontrivial topology. *Nat. Commun.* **5**, 4898 (2014).
16. M. Yan et al., Lorentz-violating type-II Dirac fermions in transition metal dichalcogenide $PtTe_2$. *Nat. Commun.* **8**, 1–6 (2017).
17. H. Hübener, M. A. Sentef, U. De Giovannini, A. F. Kemper, A. Rubio, Creating stable Floquet-Weyl semimetals by laser-driving of 3D Dirac materials. *Nat. Commun.* **8**, 13940 (2017).
18. M. S. Bahramy et al., Ubiquitous formation of bulk Dirac cones and topological surface states from a single orbital manifold in transition-metal dichalcogenides. *Nat. Mater.* **17**, 21–28 (2018).
19. F. Fei et al., Band structure perfection and superconductivity in type-II Dirac semimetal $Ir_{1-x}Pt_xTe_2$. *Adv. Mater.* **30**, 1801556 (2018).
20. Y. Cao et al., Unconventional superconductivity in magic-angle graphene superlattices. *Nature* **556**, 43–50 (2018).
21. Y. Cao et al., Correlated insulator behaviour at half-filling in magic-angle graphene superlattices. *Nature* **556**, 80–84 (2018).
22. L. Ye et al., Massive Dirac fermions in a ferromagnetic kagome metal. *Nature* **555**, 638–642 (2018).
23. J. X. Yin et al., Giant and anisotropic many-body spin-orbit tunability in a strongly correlated kagome magnet. *Nature* **562**, 91–95 (2018).
24. X. Qian, J. Liu, L. Fu, J. Li, Solid state theory. Quantum spin Hall effect in two-dimensional transition metal dichalcogenides. *Science* **346**, 1344–1347 (2014).
25. L. Tarruell, D. Greif, T. Uehlinger, G. Jotzu, T. Esslinger, Creating, moving and merging Dirac points with a Fermi gas in a tunable honeycomb lattice. *Nature* **483**, 302–305 (2012).
26. M. Milićević et al., Type-III and tilted Dirac cones emerging from flat bands in photonic orbital graphene. *Phys. Rev. X* **9**, 031010 (2019).
27. G. Montambaux, L. K. Lim, J. N. Fuchs, F. Piéchon, Winding vector: How to annihilate two Dirac points with the same charge. *Phys. Rev. Lett.* **121**, 256402 (2018).
28. Gonçalves M, Ribeiro P, Castro EV, Dirac points merging and wandering in a model Chern insulator. *EPL* **124**, 67003 (2019).
29. H. Hübener et al., Engineering quantum materials with chiral optical cavities. *Nat. Mater.* **20**, 438–442 (2021).
30. D. M. Kennes et al., Moiré heterostructures: A condensed matter quantum simulator. *Nat. Phys.* **17**, 155–163 (2021).
31. S. Pakhira, J. L. Mendoza-Cortes, Tuning the Dirac cone of bilayer and bulk structure graphene by intercalating first row transition metals using first-principles calculations. *J. Phys. Chem. C* **122**, 4768–4782 (2018).
32. Y. Tsujikawa et al., Controlling of the Dirac band states of Pb-deposited graphene by using work function difference. *AIP Adv.* **10**, 085314 (2020).
33. S. Roy et al., Tuning the Dirac point position in Bi(2)Se(3)(0001) via surface carbon doping. *Phys. Rev. Lett.* **113**, 116802 (2014).
34. Miao L et al., Observation of a topological insulator Dirac cone reshaped by non-magnetic impurity resonance. *npj Quantum Mater.* **3**, 1–7 (2018).
35. D. Galanakis, T. D. Stanescu, Electrostatic effects and band bending in doped topological insulators. *Phys. Rev. B* **86**, 195311 (2012).
36. A. Díaz-Fernández, L. Chico, J. W. González, F. Domínguez-Adame, Tuning the Fermi velocity in Dirac materials with an electric field. *Sci. Rep.* **7**, 8058 (2017).
37. A. Díaz-Fernández, E. Díaz, A. Gómez-León, G. Platero, F. Domínguez-Adame, Floquet engineering of Dirac cones on the surface of a topological insulator. *Phys. Rev. B* **100**, 075412 (2019).
38. B. Zhou et al., Controlling the carriers of topological insulators by bulk and surface doping. *Semicond. Sci. Technol.* **27**, 124002 (2012).
39. T. Sato et al., Evolution of metallic states from the Hubbard band in the two-dimensional Mott system $BaCo_{1-x}Ni_xS_2$. *Phys. Rev. B Condens. Matter Mater. Phys.* **64**, 075103 (2001).
40. L. S. Martinson, J. W. Schweitzer, N. C. Baenziger, Metal-insulator transitions in $BaCo_{1-x}N_xS_{2-y}$. *Phys. Rev. Lett.* **71**, 125 (1993).
41. S. Krishnakumar, T. Saha-Dasgupta, N. Shanthi, P. Mahadevan, D. Sarma, Electronic structure of and covalency driven metal-insulator transition in $BaCo_{1-x}Ni_xS_2$. *Phys. Rev. B Condens. Matter Mater. Phys.* **63**, 045111 (2001).
42. D. Mandrus et al., Magnetism in $BaCoS_2$. *J. Appl. Phys.* **81**, 4620–4622 (1997).
43. D. Santos-Cottin et al., Linear behavior of the optical conductivity and incoherent charge transport in $BaCoS_2$. *Phys. Rev. Mater.* **2**, 105001 (2018).
44. D. Santos-Cottin et al., Anomalous metallic state in quasi-two-dimensional $BaNiS_2$. *Phys. Rev. B* **93**, 125120 (2016).
45. I. E. Grey, H. Steinfink, Crystal structure and properties of barium nickel sulfide, a square-pyramidal nickel (II) compound. *J. Am. Chem. Soc.* **92**, 5093 (1970).
46. Y. Kim, B. J. Wieder, C. L. Kane, A. M. Rappe, Dirac line nodes in inversion-symmetric crystals. *Phys. Rev. Lett.* **115**, 036806 (2015).
47. R. Yu, H. Weng, Z. Fang, X. Dai, X. Hu, Topological node-line semimetal and Dirac semimetal state in antiperovskite Cu_3PdN. *Phys. Rev. Lett.* **115**, 036807 (2015).
48. L. S. Xie et al., A new form of Ca_3P_2 with a ring of Dirac nodes. *APL Mater.* **3**, 083602 (2015).
49. L. M. Schoop et al., Dirac cone protected by non-symmorphic symmetry and three-dimensional Dirac line node in ZrSiS. *Nat. Commun.* **7**, 11696 (2016).
50. N. Nilforoushan et al., Photoinduced renormalization and electronic screening of quasi-two-dimensional Dirac states in $BaNiS_2$. *Phys. Rev. Research* **2**, 043397 (2020).
51. Y. Klein et al., Importance of nonlocal electron correlation in the $BaNiS_2$ semimetal from quantum oscillations studies. *Phys. Rev. B* **97**, 075140 (2018).
52. I. Hase, N. Shirakawa, Y. Nishihara, Electronic structures of $BaNiS_2$ and $BaCoS_2$. *J. Phys. Soc. Jpn.* **64**, 2533–2540 (1995).
53. D. Santos-Cottin et al., Rashba coupling amplification by a staggered crystal field. *Nat. Commun.* **7**, 11258 (2016).
54. V. Cvetkovic, O. Vafek, Space group symmetry, spin-orbit coupling, and the low-energy effective Hamiltonian for iron-based superconductors. *Phys. Rev. B Condens. Matter Mater. Phys.* **88**, 134510 (2013).
55. L. de' Medici, J. Mravlje, A. Georges, Janus-faced influence of Hund's rule coupling in strongly correlated materials. *Phys. Rev. Lett.* **107**, 256401 (2011).

APPLIED PHYSICAL SCIENCES

Nilforoushan et al.
Moving Dirac nodes by chemical substitution

PNAS | 7 of 8
https://doi.org/10.1073/pnas.2108617118

56. P. Liu *et al.*, Electron and hole doping in the relativistic Mott insulator Sr_2IrO_4: A first-principles study using band unfolding technique. *Phys. Rev. B* **94**, 195145 (2016).

57. D. Carpentier, A. A. Fedorenko, E. Orignac, Effect of disorder on 2D topological merging transition from a Dirac semi-metal to a normal insulator. *EPL* **102**, 67010 (2013).

58. C. Bigi *et al.*, Very efficient spin polarization analysis (VESPA): New exchange scattering-based setup for spin-resolved ARPES at APE-NFFA beamline at Elettra. *J. Synchrotron Radiat.* **24**, 750–756 (2017).

59. M. Caputo *et al.*, Dynamics of out-of-equilibrium electron and hole pockets in the type-II Weyl semi-metal candidate WTe_2. *Phys. Rev. B* **97**, 115115 (2018).

60. P. Dudin *et al.*, Angle-resolved photoemission spectroscopy and imaging with a submicrometre probe at the SPECTROMICROSCOPY-3.2L beamline of Elettra. *J. Synchrotron Radiat.* **17**, 445–450 (2010).

61. J. P. Perdew, K. Burke, M. Ernzerhof, Generalized gradient approximation made simple. *Phys. Rev. Lett.* **77**, 3865–3868 (1996).

62. J. P. Perdew, K. Burke, M. Ernzerhof, Generalized gradient approximation made simple [Phys. Rev. Lett. 77, 3865 (1996)]. *Phys. Rev. Lett.* **78**, 1396 (1996).

63. P. Giannozzi *et al.*, QUANTUM ESPRESSO: A modular and open-source software project for quantum simulations of materials. *J. Phys. Condens. Matter* **21**, 395502 (2009).

64. P. Giannozzi *et al.*, Advanced capabilities for materials modelling with Quantum ESPRESSO. *J. Phys. Condens. Matter* **29**, 465901 (2017).

65. L. Lin, Adaptively compressed exchange operator. *J. Chem. Theory Comput.* **12**, 2242–2249 (2016).

66. A. A. Mostofi *et al.*, wannier90: A tool for obtaining maximally-localised Wannier functions. *Comput. Phys. Commun.* **178**, 685–699 (2008).

67. R. Dovesi *et al.*, Quantum-mechanical condensed matter simulations with CRYSTAL. *Wiley Interdiscip. Rev. Comput. Mol. Sci.* **8**, e1360 (2018).

68. M. Burkatzki, C. Filippi, M. Dolg, Energy-consistent small-core pseudopotentials for 3d-transition metals adapted to quantum Monte Carlo calculations. *J. Chem. Phys.* **129**, 164115 (2008).